Neural Network Approach for Characterizing Structural Transformations by X-Ray Absorption Fine Structure Spectroscopy

Janis Timoshenko,[1,*] Andris Anspoks,[2] Arturs Cintins,[2] Alexei Kuzmin,[2] Juris Purans,[2] and Anatoly I. Frenkel[1,3,†]
[1]*Department of Materials Science and Chemical Engineering, Stony Brook University, Stony Brook, New York 11794, USA*
[2]*Institute of Solid State Physics, University of Latvia, Kengaraga Street 8, Riga, LV-1063, Latvia*
[3]*Division of Chemistry, Brookhaven National Laboratory, Upton, New York 11973, USA*

(Received 23 February 2018; published 31 May 2018)

The knowledge of the coordination environment around various atomic species in many functional materials provides a key for explaining their properties and working mechanisms. Many structural motifs and their transformations are difficult to detect and quantify in the process of work (operando conditions), due to their local nature, small changes, low dimensionality of the material, and/or extreme conditions. Here we use an artificial neural network approach to extract the information on the local structure and its *in situ* changes directly from the x-ray absorption fine structure spectra. We illustrate this capability by extracting the radial distribution function (RDF) of atoms in ferritic and austenitic phases of bulk iron across the temperature-induced transition. Integration of RDFs allows us to quantify the changes in the iron coordination and material density, and to observe the transition from a body-centered to a face-centered cubic arrangement of iron atoms. This method is attractive for a broad range of materials and experimental conditions.

DOI: 10.1103/PhysRevLett.120.225502

Local deviations of atomic positions from periodic lattice sites often result in unique structural motifs and functionalities in both bulk [1–4] and nanomaterials [5–7]. Local atomic displacements are also crucial in many processes, such as chemical reactions and phase transitions, and are often a key for explaining the properties and working mechanisms in functional materials [2,8–14]. If correlation lengths for local distortions are shorter than the size of the coherent scattering region, these processes are difficult to observe by methods sensitive to long-range order [4,6]. Additional challenges for detection and interpretation of structural transformations arise because they are often associated with low concentration or low dimensionality of the material, as well as high temperature or high pressure. In many cases the actual atomic displacements are also quite subtle, not exceeding 0.1–0.2 Å.

Extended x-ray absorption fine structure (EXAFS) spectroscopy has excellent sensitivity to local atomic displacements (with accuracy 0.01 Å and better), elemental specificity, and sensitivity to vibrational dynamics [15,16]. EXAFS can be acquired in a broad range of experimental conditions; thus, this technique is well suited for *in situ* studies of structural transformations [8,9,13,14,17–22]. New approaches are sought for extending the use of EXAFS beyond its most common application: analysis of the first few coordination shells and moderately ordered materials [23].

The ability to recognize patterns and correlations in large data sets provided by recent progress in machine learning (ML) [24–26] offers new opportunities for extracting "hidden" information on local structure from experimental data. We have recently demonstrated that ML allows extraction of structure descriptors in nanoparticles from their x-ray absorption near edge structure (XANES) [27]. Here we develop an approach for the interpretation of structural transitions and disorder effects in EXAFS data, to which sensitivity of XANES is limited. As we show in this Letter, ML enables direct interpretation of EXAFS features in bulk and nanostructured materials in terms of atomistic radial distribution function (RDF) without assuming a particular disorder model. Furthermore, it allows RDF extraction in the longer range of interatomic distances, compared to conventional analysis.

We illustrate our method on the example of bulk iron undergoing temperature-induced phase transition. At temperature ~1190 K the body-centered cubic structure (bcc) of iron α phase (ferrite) changes to a face-centered cubic structure (fcc) of γ phase (austenite) [28]. This phase transformation is an integral part of many technological processes [10,29,30], but its mechanism is far from being understood due to the experimental challenges in accurate characterization of the local structure changes [29,31,32]. While a few high-pressure studies of iron appeared recently [13,14,20–22], no EXAFS studies of high-temperature bcc-to-fcc phase transition were reported, which can be attributed both to the difficulties of experimental measurements at such high temperature, and the corresponding challenges in EXAFS analysis. The latter problem is universal: at high temperatures EXAFS amplitude is reduced significantly by enhanced disorder effects, while

 © 2018 American Physical Society

anharmonicity of atomic thermal motion results in complex, asymmetric bond lengths distributions that are difficult to account for [23]. These challenges are common for many structural transformations. As we will demonstrate, the ML-based approach allows reliable extraction of the structural information on the short- and medium-range order at temperatures as high as 1300 K.

RDF $g(R)$ is a key descriptor of local structure. Following changes in RDF one can detect and characterize the phase transitions [33–35], alloying [36,37], structural motifs, and their transformations in nanoparticles [38,39]. EXAFS $\chi(k)$ (here k is the photoelectron wave number) can be expanded as $\chi(k) = \sum_p \chi^p(k)$, where summation includes single-scattering and multiple-scattering (MS) contributions. For single scattering [15]

$$\chi^p(k) = \int_0^{+\infty} S_0^2 A_p(k,R) g_p(R) \sin[2kR + \phi_p(k,R)] \frac{dR}{R^2}, \tag{1}$$

where $S_0^2 A_p$ and ϕ_p are the scattering amplitude and phase functions and $g_p(R)$ is partial RDF, corresponding to a specific coordination shell. Equation (1) can be generalized to include MS contributions by replacing $g_p(R)$ with corresponding many-atomic distribution functions [40].

Reconstruction of RDF from EXAFS spectra is an ill-posed problem, and relies on additional constraints and assumptions, such as (i) the shape of RDF peaks in conventional fitting approaches [41–43], (ii) the knowledge of the initial structure model and density of material in reverse Monte Carlo (RMC) simulations [44–46], and (iii) the non-negativity and smoothness of the RDF in regularizationlike techniques [43,47,48]. The constraints that work well for one material do not necessarily perform well for another, even less so for the transitional region between different phases. The development of constraints and fitting models is often subjective. An alternative is to rely for this purpose on a data-driven ML, where the parameters are optimized during the training stage, so that the routine gives accurate results for a broad range of relevant systems.

For extraction of RDF from EXAFS we use an artificial neural network (NN) [26,27]. The nonlinear sensitivity of NN to input features is the reason behind its unique ability to detect subtle fingerprints of local structure. NN is a composite function represented as a network of nodes, where the ith node in the nth NN layer performs a nonlinear operation on all inputs $x^{[n-1](j)}$, weighted with parameters $\theta^{[n](i,j)}$, and produces a single output $x^{[n](i)}$. By optimizing $\theta^{[n](i,j)}$, a sufficiently large NN can be trained to reproduce reliably the relationship between inputs and outputs. In our approach, illustrated in Fig. 1, an EXAFS spectrum is used to set the node values in the NN input layer [Fig. 1(a)]. Here, instead of discretizing EXAFS in k space, or Fourier

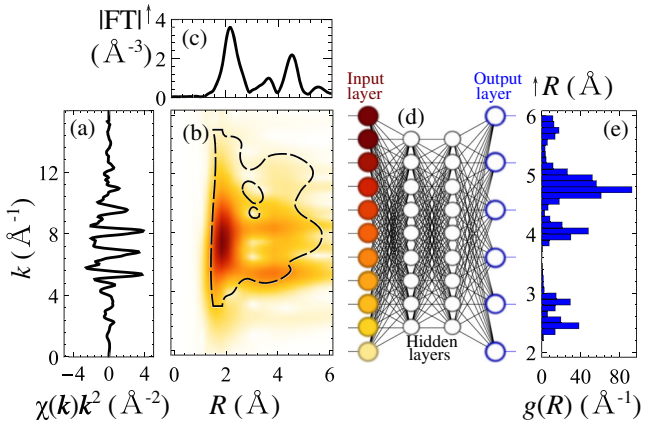

FIG. 1. Fe K-edge EXAFS for bcc iron (a). Modulus of its Morlet WT is shown in (b), while the modulus of Fourier transform (FT) is shown in (c). The dashed line in (b) indicates the region in k and R space, established as the most sensitive to structure variations. WT data are processed by NN (d), to map features in wavelet-transformed spectra to the features in RDF, approximated with a histogram (e).

transforming it to frequency (R) space [Fig. 1(c)], we employ wavelet transformation (WT) [Fig. 1(b)] [49,50], which represents EXAFS spectrum in k and R spaces simultaneously. Only the WT points that are sensitive to structure changes are used: this region in k and R space is shown in Fig. 1(b), and is obtained automatically based on the analysis of variations in the training spectra. The wavelet-transformed spectra are then processed by the nodes in the NN further layers [Fig. 1(d)]. The output layer of the NN produces a vector, which encodes the entire RDF [Fig. 1(e)], approximated with a histogram in a given R range between $R_{\min}$ and $R_{\max}$: each NN output node yields the height of a particular histogram bin.

The crucial part of NN analysis is the training process. Here, we supply as input to the NN a set of EXAFS spectra χ_t, for which the corresponding RDFs $g_t(R)$ are known. This true $g_t(R)$ is compared with the NN output $\tilde{g}_t(R)$, and the NN weights $\theta^{[n](i,j)}$ are updated, so that the difference between $\tilde{g}_t(R)$ and $g_t(R)$ is minimized for all training spectra. It is not feasible to construct such a training set based on experimental measurements. Note also that to have a reliable, unbiased NN, the training set should represent a large portion of configurational space, not limited to a relatively small number of experimentally available structures. To solve this problem we use classical molecular dynamics (MD) to create ~3000 training examples, corresponding to different phases of iron and different degrees of disorder. Knowing the atomic trajectories in MD simulations, we calculate the corresponding RDFs, as well as the corresponding time- and ensemble-averaged EXAFS (MD-EXAFS). As we have demonstrated before [46,51–53], MD allows one to generate EXAFS spectra in a qualitative agreement with experimental data. A very accurate agreement between MD-EXAFS and experimental

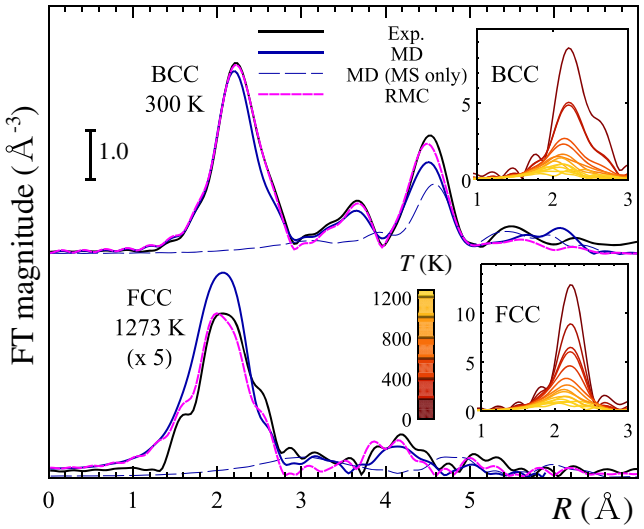

FIG. 2. Fourier-transformed experimental and simulated (with MD and RMC methods) Fe K-edge EXAFS for bulk iron at 300 and 1273 K temperatures. Contribution of MS paths to the total MD-EXAFS is shown separately. Spectra corresponding to 1273 K are shifted vertically and multiplied by 5. Insets show the temperature dependencies of MD-EXAFS for bcc and fcc structures (only the main FT-EXAFS peak).

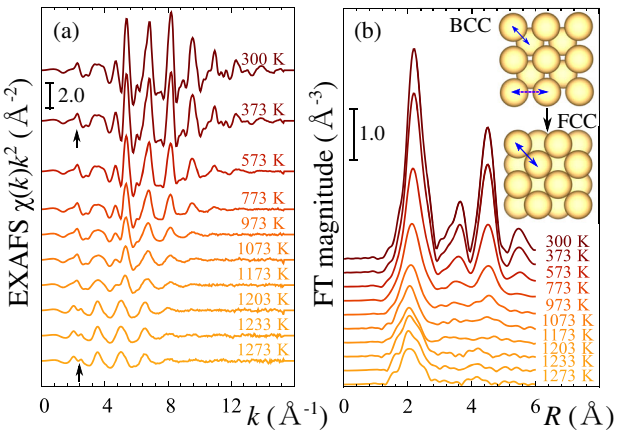

FIG. 3. Experimental Fe K-edge EXAFS in k space (a) and R space (b) for temperatures between 300 and 1273 K. Arrows in (a) indicate the features in the low k range, whose change implies the phase transition from the bcc to fcc structure [inset in (b)]. Arrows in the inset show the atomic pairs contributing to the main FT-EXAFS peak in both structures.

EXAFS is not required here, since MD-EXAFS data are used solely for the purpose of establishing the relation between EXAFS and RDF features, and not for direct matching with experimental data [52]. For MD we used Sutton-Chen type potential [54]. To calculate MD-EXAFS spectra (Fig. 2) we used the same procedure as in Refs. [46,52]. MD simulations were carried out for iron with bcc, fcc, and hexagonal close-packed (hcp) structures in the temperature range from 10 up to 1500 K. Figure 2 compares the calculated MD-EXAFS with the experimental data for bcc iron at room temperature [Fig. 2(a)] and fcc iron at 1273 K [Fig. 2(b)]. MD describes reasonably the experimental room temperature EXAFS, and gives qualitative agreement with the high temperature data. In the latter case the disorder in the first coordination shell is underestimated in simulations, as evidenced by the higher main FT peak. The temperature-dependent MD-EXAFS spectra are shown in the insets and were used for NN training, and also for validation of its accuracy [see Supplemental Material (Figs. S1 and S2)] [55].

The experimental Fe K-edge EXAFS, reported in Fig. 2, were recorded *in situ* in transmission mode at the ELETTRA synchrotron [66]. A 40% detuned Si (111) double-crystal monochromator was used. The intensities of the incident and transmitted x-ray beams were measured by two ionization chambers filled with argon and krypton gases. High purity iron foil (Goodfellow, 99.99+%) with the thickness of 4 μm was used as a sample. The sample temperature was controlled in the range from 300 to 1273 K using the L'Aquila-Camerino vacuum glass furnace [67]. To avoid any contact with the graphite foil heater of the furnace (the graphite was necessary for transmission x-ray experiment) and to prevent the sample from oxidation and carbidization that plague most high temperature experiments with pure iron, the sample was gently packed between two BN pellets. Note that BN is thermally stable up to ~3200 K [68], but reacts with iron at ~1400 K [69].

Temperature dependencies of the obtained experimental spectra are shown in Fig. 3. The good signal-to-noise ratio is observed in the k-space data [Fig. 3(a)] even at the highest temperature. The lack of features at low R values (around ~1 Å) in Fourier-transformed data [Fig. 3(b)] together with the stability of all XANES features (Supplemental Material, Fig. S3) give us confidence that the metallic state of iron is preserved in our measurements.

An indirect indication of the transition from a bcc to a fcc structure [see the inset in Fig. 3(b)] is the change in the features at low k values, marked in Fig. 3(a). These features cannot be included in EXAFS analysis due to the artifacts of background subtraction and inaccuracies of EXAFS theory in this region. The changes in features at higher k values ($k > 3$ Å) and in R space are subtler and masked by the temperature effect. In particular, both bcc and fcc structures yield a single nearest neighbor peak to the R-space spectrum between ca 1.5 and 3 Å, Fig. 3(b). It is known, however, that these two structures have different nearest neighbor RDFs: in the ideal bcc structure with lattice constant a_0 each atom is surrounded by 8 atoms at the distance $a_0\sqrt{3}/2$, and 6 atoms at the distance a_0. In the ideal fcc structure all atoms are surrounded by 12 nearest neighbors at the same distance $a_0/\sqrt{2}$. The corresponding pairs of atoms are shown in the inset of Fig. 3(b).

In Fig. 4 we apply NN, trained on MD-EXAFS spectra, to the analysis of experimental data. RDFs, reconstructed by NN from experimental Fe K-edge EXAFS in bulk iron

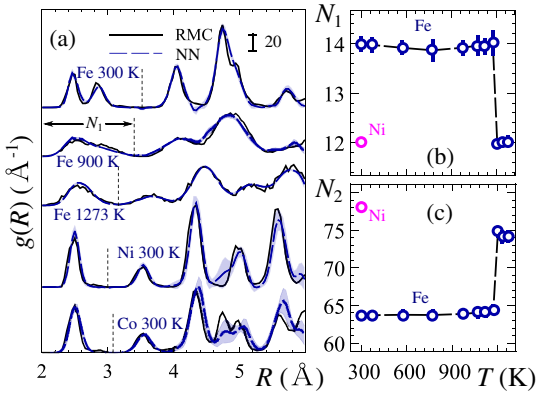

FIG. 4. (a) RDFs for iron at 300, 900, and 1273 K, and for nickel (fcc) and cobalt (hcp), obtained by NN from experimental EXAFS. Dashed line is the averaged result from 10 independently trained NNs, shaded regions show the standard deviation of these results and characterize the uncertainty. For comparison the results of RMC simulations are also shown. The R_1 value is shown as a vertical dashed line. Temperature dependencies of integrated RDFs N_1 and N_2 are shown with empty circles in (b) and (c). Dashed lines are a guide for the eye.

are shown in Fig. 4(a) (for selected temperatures) and in the Supplemental Material, Fig. S4. The obtained RDFs $\tilde{g}(R)$ are smooth and non-negative functions for all values of R. As expected, at low temperature the RDF between 2 and 4 Å is split in two peaks, in agreement with the bcc-type structure. At higher temperatures, RDF peaks broaden and merge together. To analyze quantitatively the obtained RDFs and to detect bcc-to-fcc phase transition, we calculated the running coordination number $N_{\mathrm{RCN}}(R) = \int_0^R \tilde{g}(r)dr$ [70]. $N_{\mathrm{RCN}}(R)$ yields a plateau in between coordination shells, which can be used to calculate the coordination numbers N of a single shell or a group of adjacent shells. For example, $N_1 = N_{\mathrm{RCN}}(R_1)$, where R_1 is the minimum of $\tilde{g}(R)$ in the R range between 2.5 and 3.5 Å, includes contribution of the first coordination shell for fcc iron, and first two coordination shells in bcc iron; thus, it is equal to 12 in fcc-type and $8 + 6 = 14$ in bcc-type material. The obtained temperature dependence of N_1 is shown in Fig. 4(b), and demonstrates a sharp transition from a bcc-like to a fcc-like environment between 1173 and 1203 K. Simultaneously, the average density of the structure sharply increases, as evidenced by the integrated contribution of distant coordination shells $N_2 = N_{\mathrm{RCN}}(R_{\mathrm{max}})$ [Fig. 4(c)]. Sharp transformation from a bcc-like to denser fcc-like structure in both cases agrees with the expected behavior for structure parameters in the first-order phase transition [29].

In summary of this part, the NN approach succeeded to obtain local structure information in iron in the broad temperature range and with much better detail than conventional EXAFS analysis. While the construction of the training sets took days of CPU time and the training of NN took hours, the calculation of the RDF for any given EXAFS spectrum using the prebuilt NN took only a few seconds. As an additional validation of our NN-based method, we performed RMC simulations, as described in Refs. [46,50], to independently obtain the RDF. Unlike it is for our NN method, RMC simulations require several CPU weeks of calculations for each EXAFS spectrum and *a priori* knowledge of crystallographical structure: here for choosing between bcc and fcc models we use NN results, while the lattice parameters were taken from Ref. [28]. The agreement between the RMC-modeled and experimental EXAFS is shown in Fig. 2 and demonstrates the high accuracy of the RMC-generated structure models both at room temperature (bcc structure) and high temperature (fcc structure). On the other hand, it shows that our experimental EXAFS data agree with the average structure model from XRD [28], and is also a testimony to the success of our experimental procedure that we used to ensure that no unwanted Fe species are present in our sample.

The RDFs, obtained from NN analysis, are compared with RMC results in Fig. 4 and Fig. S4, and confirm the high accuracy of our NN-based method: even at the highest temperature the asymmetric shapes of RDF peaks up to 6 Å are reproduced reliably by NN. Note that the current 6 Å limit is imposed only by the number of photoelectron paths, included in EXAFS calculations, and our analysis, in principle, can be extended to even more distant coordination shells.

Another important point is that NN-based analysis performs substantially better than a trivial matching of theoretical spectra with experimental data. One may imagine that instead of being used for NN training, MD-EXAFS data could be compared directly with experimental EXAFS, and the RDF for the model that gives the best agreement with experiment is then claimed to be the true RDF in the experimental sample. Results of such a matching approach are shown in Fig. S4. While it gives comparable results to our NN method at low temperatures, it fails at higher temperatures, where in an attempt to describe the temperature effect in the dominating first coordination shell contribution it allows significant inaccuracies in the contributions of distant coordination shells.

Since in bulk iron the fcc structure is observed only at high temperature, to demonstrate the ability of our method to recognize well-ordered low-temperature fcc-type structures, we apply it to Ni K-edge EXAFS in bulk Ni, which has fcc structure at room temperature (Fig. 4). Let us clarify here that our NN was trained on theoretical Fe K-edge spectra only. However, since Ni and Fe are neighbors in the periodic table, their photoelectron scattering properties are close, and one can use the NN, trained on iron data, to analyze nickel data as well. As shown in Fig. 4, our NN correctly predicts the fcc-type structure for Ni, and the shapes of RDF peaks are in an excellent agreement with RMC results. One can also find the one-to-one correspondence between the RDF features in the result for Ni at room temperature and Fe at high temperature. Similar reasoning

allows us to employ our NN to analyze Co K-edge EXAFS from bulk cobalt that, at room temperature, assumes the hcp-type structure. As shown in Fig. 4, NN gives excellent results in this case as well. Importantly, it can detect the splitting of the RDF peak between ~4.5 and 5.0 Å, which distinguishes the RDF of hcp-type cobalt from that of the fcc-type Ni. The ability of our NN to detect the differences between the fcc and hcp structures from EXAFS spectra is remarkable, since it is almost impossible to detect this subtle difference by other approaches to EXAFS analysis.

To summarize, the neural network-based method enables accurate and fast extraction of structural information from experimental EXAFS. The advantage of this approach over existing analysis methods was demonstrated on the example of the *in situ* study of high-temperature structural transition from ferrite to austenite. The NN-based method can immediately be applied to the local structure analyses in Fe, Ni, Co, and Mn metals, as well as in their alloys. It can also be easily generalized to other systems (including nonmetallic, multicomponent materials). We envision that an important application of this method will be *in situ* monitoring of structural transformations in nanostructured materials. We believe also that the method, developed here for deciphering EXAFS spectra, will be useful for the analysis of other structure-sensitive data, e.g., for analysis of pair-distribution functions from the total x-ray or neutron scattering data [33,71], where one faces similar challenges in data analysis as in EXAFS spectroscopy. The trained NNs can be shared (since they are explicit functions), and we anticipate that an openly available library of NNs, trained for specific tasks (e.g., processing of EXAFS and XANES data in different materials) can be developed, allowing the researchers in the field to analyze their own data without the need to do the tedious NN training process themselves.

A. I. F. acknowledges support by the U.S. Department of Energy, Office of Basic Energy Sciences under Grant No. DE-FG02-03ER15476. A. I. F. acknowledges support by the Laboratory Directed Research and Development Program through LDRD 18-047 of Brookhaven National Laboratory under U.S. Department of Energy Contract No. DE-SC0012704 for initiating his research in machine learning methods. The help of the beam line staff at ELETTRA (Project No. 20160412) synchrotron radiation facility is acknowledged. RMC-EXAFS and MD-EXAFS simulations were performed on the LASC cluster-type computer at Institute of Solid State Physics of the University of Latvia.

*janis.timosenko@stonybrook.edu
†anatoly.frenkel@stonybrook.edu

[1] R. E. Cohen, Nature (London) **358**, 136 (1992).
[2] I. Levin, V. Krayzman, and J. C. Woicik, Phys. Rev. B **89**, 024106 (2014).
[3] E. Aksel, J. S. Forrester, J. C. Nino, K. Page, D. P. Shoemaker, and J. L. Jones, Phys. Rev. B **87**, 104113 (2013).
[4] R. Comes, M. Lambert, and A. Guinier, Solid State Commun. **6**, 715 (1968).
[5] P. Moriarty, Rep. Prog. Phys. **64**, 297 (2001).
[6] S. J. Billinge and I. Levin, Science **316**, 561 (2007).
[7] F. Fischer, T. Waitz, D. Vollath, and N. Simha, Prog. Mater. Sci. **53**, 481 (2008).
[8] E. A. Stern and K. Zhang, Phys. Rev. Lett. **60**, 1872 (1988).
[9] E. A. Stern, P. Livins, and Z. Zhang, Phys. Rev. B **43**, 8850 (1991).
[10] K. Kadau, T. C. Germann, P. S. Lomdahl, and B. L. Holian, Science **296**, 1681 (2002).
[11] F. F. Tao and M. Salmeron, Science **331**, 171 (2011).
[12] W. Wełnic, A. Pamungkas, R. Detemple, C. Steimer, S. Blügel, and M. Wuttig, Nat. Mater. **5**, 56 (2006).
[13] O. Mathon, F. Baudelet, J. P. Itié, A. Polian, M. d'Astuto, J. C. Chervin, and S. Pascarelli, Phys. Rev. Lett. **93**, 255503 (2004).
[14] Y. Ping, F. Coppari, D. Hicks, B. Yaakobi, D. Fratanduono, S. Hamel, J. Eggert, J. Rygg, R. Smith, D. Swift *et al.*, Phys. Rev. Lett. **111**, 065501 (2013).
[15] E. Stern, in *X-Ray Absorption: Principles, Applications, Techniques of EXAFS, SEXAFS, and XANES*, edited by D. Koningsberger and R. Prins (John Wiley and Sons, New York, NY, 1988), Chap. 1, p. 3.
[16] J. Purans, N. D. Afify, G. Dalba, R. Grisenti, S. De Panfilis, A. Kuzmin, V. I. Ozhogin, F. Rocca, A. Sanson, S. I. Tiutiunnikov *et al.*, Phys. Rev. Lett. **100**, 055901 (2008).
[17] D. R. Sandstrom and F. W. Lytle, Annu. Rev. Phys. Chem. **30**, 215 (1979).
[18] R. Prins and D. Koningsberger, in *X-Ray Absorption: Principles, Applications, Techniques of EXAFS, SEXAFS, and XANES*, edited by D. Koningsberger and R. Prins (John Wiley and Sons, New York, NY, 1988), Chap. 8, p. 321.
[19] F. M. Wang and R. Ingalls, Phys. Rev. B **57**, 5647 (1998).
[20] B. Yaakobi, T. R. Boehly, D. D. Meyerhofer, T. J. B. Collins, B. A. Remington, P. G. Allen, S. M. Pollaine, H. E. Lorenzana, and J. H. Eggert, Phys. Rev. Lett. **95**, 075501 (2005).
[21] G. Aquilanti, A. Trapananti, A. Karandikar, I. Kantor, C. Marini, O. Mathon, S. Pascarelli, and R. Boehler, Proc. Natl. Acad. Sci. U.S.A. **112**, 12042 (2015).
[22] R. Torchio, F. Occelli, O. Mathon, A. Sollier, E. Lescoute, L. Videau, T. Vinci, A. Benuzzi-Mounaix, J. Headspith, W. Helsby *et al.*, Sci. Rep. **6**, 26402 (2016).
[23] E. D. Crozier, J. J. Rehr, and R. Ingalls, in *X-Ray Absorption: Principles, Applications, Techniques of EXAFS, SEXAFS, and XANES*, edited by D. Koningsberger and R. Prins (John Wiley and Sons, New York, NY, 1988), Chap. 9, p. 373.
[24] L. Wang, Phys. Rev. B **94**, 195105 (2016).
[25] Q. Zhu, A. Samanta, B. Li, R. E. Rudd, and T. Frolov, Nat. Commun. **9**, 467 (2018).
[26] P. Zhang, H. Shen, and H. Zhai, Phys. Rev. Lett. **120**, 066401 (2018).
[27] J. Timoshenko, D. Lu, Y. Lin, and A. I. Frenkel, J. Phys. Chem. Lett. **8**, 5091 (2017).
[28] Z. Basinski, W. Hume-Rothery, and A. Sutton, Proc. R. Soc. A **229**, 459 (1955).

[29] G. L. Krasko and G. B. Olson, Phys. Rev. B **40**, 11536 (1989).
[30] S. V. Okatov, A. R. Kuznetsov, Y. N. Gornostyrev, V. N. Urtsev, and M. I. Katsnelson, Phys. Rev. B **79**, 094111 (2009).
[31] X. Ou, Mater. Sci. Technol. **33**, 822 (2017).
[32] C. Bos, J. Sietsma, and B. J. Thijsse, Phys. Rev. B **73**, 104117 (2006).
[33] S. Billinge and G. Kwei, J. Phys. Chem. Solids **57**, 1457 (1996).
[34] Y. Katayama, T. Mizutani, W. Utsumi, O. Shimomura, M. Yamakata, and K.-i. Funakoshi, Nature (London) **403**, 170 (2000).
[35] Y. Shibuta and T. Suzuki, J. Chem. Phys. **129**, 144102 (2008).
[36] F. Calvo, E. Cottancin, and M. Broyer, Phys. Rev. B **77**, 121406 (2008).
[37] A. I. Frenkel, Chem. Soc. Rev. **41**, 8163 (2012).
[38] D. Glasner and A. I. Frenkel, AIP Conf. Proc. **882**, 746 (2007).
[39] A. I. Frenkel, M. W. Small, J. G. Smith, R. G. Nuzzo, K. O. Kvashnina, and M. Tromp, J. Phys. Chem. C **117**, 23286 (2013).
[40] A. Filipponi, A. Di Cicco, and C. R. Natoli, Phys. Rev. B **52**, 15122 (1995).
[41] G. Bunker, Nucl. Instrum. Methods Phys. Res. **207**, 437 (1983).
[42] M. Newville, J. Synchrotron Radiat. **8**, 96 (2001).
[43] A. Kuzmin and J. Chaboy, IUCrJ **1**, 571 (2014).
[44] S. Gurman and R. McGreevy, J. Phys. Condens. Matter **2**, 9463 (1990).
[45] A. Di Cicco, A. Trapananti, S. Faggioni, and A. Filipponi, Phys. Rev. Lett. **91**, 135505 (2003).
[46] J. Timoshenko and A. I. Frenkel, Catal. Today **280**, 274 (2017).
[47] N. Ershov, A. Ageev, V. Vasin, and Y. A. Babanov, Phys. Status Solidi B **108**, 103 (1981).
[48] A. Frenkel, E. A. Stern, A. Voronel, A. Rubshtein, Y. Ben-Ezra, and V. Fleurov, Phys. Rev. B **54**, 884 (1996).
[49] J. Timoshenko and A. Kuzmin, Comput. Phys. Commun. **180**, 920 (2009).
[50] J. Timoshenko, A. Kuzmin, and J. Purans, J. Phys. Condens. Matter **26**, 055401 (2014).
[51] A. Kuzmin, A. Anspoks, A. Kalinko, and J. Timoshenko, Z. Phys. Chem. (Frankfort/Main) **230**, 537 (2016).
[52] J. Timoshenko, K. R. Keller, and A. I. Frenkel, J. Chem. Phys. **146**, 114201 (2017).
[53] I. Jonane, A. Anspoks, and A. Kuzmin, Model. Simul. Mater. Sci. Eng. **26**, 025004 (2018).
[54] X. Dai, Y. Kong, J. Li, and B. Liu, J. Phys. Condens. Matter **18**, 4527 (2006).
[55] See Supplemental Material at http://link.aps.org/supplemental/10.1103/PhysRevLett.120.225502 for technical details of MD simulations, NN implementation and training, and supplemental figures showing analysis of training spectra, validation of NN accuracy, experimental Fe *K*-edge XANES and results of NN analysis of experimental data in a broad temperature range, which includes Refs. [56–65].
[56] Wolfram Research, Inc., *Mathematica, version 11.2* (Wolfram Research Inc., Champaign, IL, 2017).
[57] A. Sutton and J. Chen, Philos. Mag. Lett. **61**, 139 (1990).
[58] J. D. Gale, Philos. Mag. B **73**, 3 (1996).
[59] J. D. Gale and A. L. Rohl, Mol. Simul. **29**, 291 (2003).
[60] S. K. Kim, C. Petersen, F. Jona, and P. M. Marcus, Phys. Rev. B **54**, 2184 (1996).
[61] W. G. Hoover, Phys. Rev. A **31**, 1695 (1985).
[62] R. W. Hockney, *Methods in Computational Physics*, edited by B. Alder, S. Fernbach, and M. Rotenberg (Academic Press, New York, 1970), Vol. 9, pp. 135–211.
[63] A. L. Ankudinov, B. Ravel, J. J. Rehr, and S. D. Conradson, Phys. Rev. B **58**, 7565 (1998).
[64] A. I. Frenkel, O. Kleifeld, S. R. Wasserman, and I. Sagi, J. Chem. Phys. **116**, 9449 (2002).
[65] J. A. Varnell, C. Edmund, C. E. Schulz, T. T. Fister, R. T. Haasch, J. Timoshenko, A. I. Frenkel, and A. A. Gewirth, Nat. Commun. **7**, 12582 (2016).
[66] A. Di Cicco, G. Aquilanti, M. Minicucci, E. Principi, N. Novello, A. Cognigni, and L. Olivi, J. Phys. Conf. Ser. **190**, 012043 (2009).
[67] A. Di Cicco, R. Gunnella, R. Marassi, M. Minicucci, R. Natali, G. Pratesi, E. Principi, and S. Stizza, J. Non-Cryst. Solids **352**, 4155 (2006).
[68] A. Liersch, H. Danninger, and R. Ratzi, Powder Metall. Prog. **7**, 66 (2007).
[69] K. P. Furlan, D. R. Consoni, B. Leite, M. V. Dias, and A. N. Klein, Microsc. Microanal. **23**, 1061 (2017).
[70] M. E. Tuckerman, *Statistical Mechanics: Theory and Molecular Simulation* (Oxford University Press, New York, 2010).
[71] B. Toby and T. Egami, Acta Crystallogr. Sect. A **48**, 336 (1992).